AIAA JOURNAL
Vol. 49, No. 4, April 2011

# Implementation of Menter's Transition Model on an Isolated Natural Laminar Flow Nacelle

Yujing Lin,* Theresa Robinson,† and Juliana Early†
*Queen's University Belfast, Belfast, Northern Ireland BT7 1NN, United Kingdom*
and
David Riordan,‡ James Tweedie,§ and Liam Magee¶
*Bombardier, Belfast, Northern Ireland BT3 9DZ, United Kingdom*

DOI: 10.2514/1.J050890

**This study evaluates the implementation of Menter's $\gamma$-$Re_\theta$ Transition Model within the CFX12 solver for turbulent transition prediction on a natural laminar flow nacelle. Some challenges associated with this type of modeling have been identified. The computational fluid dynamics transitional flow simulation results are presented for a series of cruise cases with freestream Mach numbers ranging from 0.8 to 0.88, angles of attack from −2 to 0°, and mass flow ratios from 0.60 to 0.75. These were validated with a series of wind-tunnel tests on the nacelle by comparing the predicted and experimental surface pressure distributions and transition locations. A selection of the validation cases are presented in this paper. In all cases, computational fluid dynamics simulations agreed reasonably well with the experiments. The results indicate that Menter's $\gamma$-$Re_\theta$ Transition Model is capable of predicting laminar boundary-layer transition to turbulence on a nacelle. Nonetheless, some limitations exist in both the Menter's $\gamma$-$Re_\theta$ Transition Model and in the implementation of the computational fluid dynamics model. The implementation of a more comprehensive experimental correlation in Menter's $\gamma$-$Re_\theta$ Transition Model, preferably the ones from nacelle experiments, including the effects of compressibility and streamline curvature, is necessary for an accurate transitional flow simulation on a nacelle. In addition, improvements to the computational fluid dynamics model are also suggested, including the consideration of varying distributed surface roughness and an appropriate empirical correction derived from nacelle experimental transition location data.**

## Nomenclature

| | | |
|---|---|---|
| $C_f$ | = | skin friction coefficient |
| $C_p$ | = | pressure distribution coefficient |
| Î± | = | angle of attack |
| $M$ | = | Mach number |
| mfr | = | mass flow ratio |
| $N$ | = | $N$-factor for Tollmien–Schlichting wave amplification |
| $R_t$ | = | turbulence viscosity ratio at domain inlet |
| $Re_t$ | = | transition Reynolds number based on transition onset location $x$ |
| $Re_\theta$ | = | transition Reynolds number based on momentum thickness $\theta$ |
| Tu | = | domain inlet turbulence intensity |
| Tu* | = | turbulence intensity downstream of domain inlet |
| $V$ | = | freestream velocity, m/s |
| $u$ | = | local velocity, m/s |
| $x_t$ | = | transition onset location, m |
| $x$ | = | distance from leading edge in the direction of the flow, m |
| $x^*$ | = | streamwise distance from domain inlet, m |
| $\gamma$ | = | turbulence intermittency |
| $\varepsilon$ | = | turbulence dissipation, $m^2/s^3$ |
| $\theta$ | = | boundary-layer momentum thickness, m |
| $k$ | = | turbulence kinetic energy, $m^2/s^2$ |
| $\mu$ | = | freestream viscosity, kg/ms |
| $\rho$ | = | freestream density, $kg/m^3$ |

*Subscripts*

| | | |
|---|---|---|
| $b$ | = | beginning of transition |
| $e$ | = | end of transition |
| inlet | = | domain inlet boundary |
| LE | = | nacelle leading edge |
| $t$ | = | transition onset |

Received 30 August 2010; revision received 13 December 2010; accepted for publication 14 December 2010. 

*Postdoctoral Research Assistant, Department of Mechanical and Aerospace Engineering, Ashby Building, 125 Stranmillis Road, Queen's University Belfast, Belfast, BT9 5AH.

†Lecturer, Department of Mechanical and Aerospace Engineering, Ashby Building, 125 Stranmillis Road, Queen's University Belfast, Belfast, BT9 5AH.

‡Chief Technical Engineer, Technical Engineering, Bombardier Aerospace, Airport Road, Belfast, BT3 9DZ.

§Staff Technical Engineer, Powerplant and Systems Department, Bombardier Aerospace, Airport Road, Belfast, BT3 9DZ.

¶Senior Technical Engineer, Powerplant and Systems Department, Bombardier Aerospace, Airport Road, Belfast, BT3 9DZ.

## I. Introduction

### A. Background

WITH today's ever increasing demand for air travel, the environmental impact of aircraft is becoming a major concern. As well as the challenges of noise pollution near airports, there is also the issue of $CO_2$ emissions. The environmental effects of emissions from burning fossil fuels are some of the most significant issues in the aircraft industry. The Advisory Council for Aeronautics Research in Europe (ACARE) has targeted a 50% reduction in aircraft $CO_2$ emissions, including a 20% reduction from engines alone by the year 2020 [1].

In addition to significantly improving aircraft operation and jet engine characteristics, a route to address the impact of emissions is to reduce aircraft drag for a given lift, and more specifically friction drag. One of the approaches to reduce aircraft drag is extending the portion of the airframe over which there is laminar flow. Efforts in the past have proven the potential of delivering extended laminar flows, decreased turbulent friction and a decreased flow separation region. These in turn make possible a lower drag coefficient, which offers a large potential fuel saving and consequently economic savings and improvements in environmental protection [2].

The majority of past research work into laminar flow technology has been devoted to maintaining extended laminar flow on wing

surfaces, using natural laminar flow (NLF) [3–6], active flow control [3,5,7], or a hybrid (HLFC) between the two [8–10]. However, the operational requirement of high subsonic cruising speeds requires the use of wing sweep. This complicates the design, since wing flows are fully three-dimensional and mechanisms for boundary-layer transition additional to Tollmien–Schlichting (T-S) waves are present, such as attachment line contamination and crossflow instability.

However, laminar flow technologies are also applicable to aircraft engine nacelles, and since nacelles are not required to generate lift and have negligible leading-edge sweep, the difficulties encountered in promoting and maintaining extended regions of laminar flow are fewer than for wings [11]. In addition, the engine nacelle is ideally suited to the early inclusion of extended laminar flow technology, being relatively self-contained with the possibility of application to existing airframes. In general, considering component surface area alone, the potential for drag reduction on a nacelle will be smaller than for a wing. Extended laminar flow should, however, be easier to achieve on a nacelle [12]. As engine bypass ratios increase, and hence the nacelle diameter, the proportional effect of nacelle laminar flow becomes more significant.

Some early studies have shown that large areas of laminar flow over aircraft engine nacelles offer significant savings in aircraft fuel consumption. In 1992, a European consortium managed by Rolls-Royce, including Motoren- und Turbinen-Union, Aero Engines, and the German Aerospace Centre (DLR), began flight testing of a natural laminar flow nacelle [13,14]. This program was later extended by Rolls-Royce and DLR to flight test a hybrid laminar flow control nacelle featuring boundary-layer suction and insect contamination protection. It demonstrated that, net benefits of up to 1.5% specific fuel consumption (SFC) are predicted for NLF on small to medium range civil transport aircraft. For HLFC on medium to long haul civil transport aircraft, benefits of up to 2% in SFC are possible [13].

Lamb et al. [11,15] conducted an experimental investigation to determine the effects of installing flow-through laminar flow nacelles on a high-wing transonic transport configuration. They used the Langley 16-ft transonic wind tunnel at freestream Mach numbers from 0.70 to 0.82 and angles of attack from −2.5 to 4.0°. Their results indicate that the ability to achieve laminar flow on the nacelle was not significantly altered by nacelle/pylon/wing integration on symmetrical pylons, although nacelle longitudinal position and pylon contour was shown to have an effect on the installed drag.

Favorable results have also been obtained in Younghans and Lahti's [16] investigation of high-speed proof-of-concept testing of a scale natural laminar flow nacelle model. Both isolated and installed laminar flow nacelle tests have been conducted in the Langley 16-ft transonic wind tunnel.

Few publications on the topic of computational transition prediction for laminar flow nacelles are available. However, in a feasibility study on the design of a laminar flow nacelle by Radespiel et al. [17], an extension of the 3-D DLR Euler code CEVCATS (Cell Vertex Central Averaged Time Stepping Scheme) coupled with an axisymmetric boundary-layer code was used to analyze the laminar and turbulent boundary-layer flow around an isolated laminar flow nacelle. A linear stability $e^N$ method was employed in conjunction with this to predict the transition location. In another study on the aerodynamic design of a natural laminar flow nacelle by Riedel et al. [14], the same simulation method was applied to an isolated and an installed natural laminar flow nacelle. This design was validated by flight testing.

Most investigations in the past on nacelle surface transition behavior focused on the design methodology for a laminar flow nacelle and validation by wind-tunnel tests and/or flight testing. However, the fundamental transition behavior on a nacelle surface, including the effect of nacelle surface profile, flight operating conditions (mission envelope) and surface imperfections has not been investigated theoretically and computationally to any depth. The fundamental understanding of these effects is crucial in any optimized nacelle design which includes the use of laminar flow for drag reduction. The rapid progress of computational fluid dynamics (CFD) technologies makes the transition modeling of these complex flow mechanisms and complicated geometric configurations possible today.

Therefore, a systematic computational investigation of engine nacelle aerodynamics with emphasis on natural laminar flow has been carried out within the Environmentally Friendly Engine project and the results compared with experimental data from a natural laminar flow wind-tunnel test investigation. A long duct mixed flow nacelle designed to provide an extended region of natural laminar flow was evaluated using a CFD software package, CFX12, which included Menter's $\gamma$-$Re_\theta$ Transition Model. Both cruise and off-design conditions have been considered and the effects of flight conditions and surface imperfections on transition have been explored.

A brief review of available transition prediction methods, with emphasis on Menter's $\gamma$-$Re_\theta$ Transition Model is presented in the next subsection. In Sec. II, the methodology used in this study is presented in detail. Then, the validation results analysis and assessment are shown in Sec. III. A summary and conclusions are presented in Sec. IV.

### B. Available Transition Modeling Methods

Predominant transition mechanisms include crossflow instability, Tollmien–Schlichting (T-S) waves and bypass transition. The mechanism which triggers the transition depends on the freestream turbulence level, the pressure gradient along the laminar boundary layer, the surface profile, the surface roughness and the freestream Mach number. In addition, acoustic disturbances and structural vibration can also be important. The most common transition mechanism on a vehicle in flight at high Reynolds number and low freestream turbulence levels (Tu $< 0.6\%$) is natural transition due to the growth of unstable T-S waves. If the turbulence levels, pressure gradients, or local flow unsteadiness is large, the process of natural transition is bypassed leading to rapid boundary-layer transition known as bypass transition. For high angle of attack cases on swept wings, the 3-D velocity profile causes crossflow transition. Flow separation in the laminar boundary layer leads to a very rapid growth of disturbances and to transition, which is called separation-induced transition.

There are three main methods used to model transition in industry [18]. The first is the application of low-Reynolds-number turbulence models [18–25]. These are based on transport equations, for example, turbulent kinetic energy $k$ and turbulence dissipation $\varepsilon$, using wall-damping functions of an underlying turbulence model to trigger the transition onset, which makes it compatible with modern CFD codes. The main shortcomings of this method are that it cannot reliably capture the influence of the many factors that affect transition, and it is only applied to bypass transition and therefore not suitable, in general, for external aircraft aerodynamic flows.

The second approach is the $e^N$ method. It is based on local linear stability theory and the parallel-flow assumption to calculate the growth of the disturbance amplitude from the boundary-layer neutral point to the transition location. Once the disturbance amplitude ratio exceeds the specified $N$-factor, transition is assumed to start. For isolated airfoils, the $e^N$ method has been shown to produce very good transition predictions of wind-tunnel measurements [26]. However, the $e^N$ method has limitations in that it cannot be used 1) for generic 3-D flows where the streamline direction is not aligned with the grid, and the need to track the growth of the disturbance amplitude ratio along the streamline cannot be satisfied, 2) to account for nonlinear effects, e.g., high freestream turbulence or roughness, since it is based on linear instability theory and 3) with Navier–Stokes equations because typical CFD codes are not accurate enough to evaluate stability equations, and therefore it is not computationally efficient [18].

The third method to predict transition is to use experimental correlation. The correlation usually relates the freestream turbulence intensity (Tu) and the local pressure gradient to the transition momentum thickness Reynolds number ($Re_{\theta t}$). A typical example is Abu–Ghannam and Shaw's correlation [27], which is based on a large number of experimental observations. The correlations can be

found for many different transition mechanisms and can take into account parameters such as freestream turbulence intensity, pressure gradients, and surface roughness. The method has been shown to be sufficiently accurate. However, one difficulty applying this transition method in industry is that it is not compatible with three-dimensional flows and unstructured/parallel CFD codes because it uses nonlocal transition criteria formulation [19].

The basic mechanism of boundary-layer transition under various flow conditions can be studied using direct numerical simulations and large eddy simulations for low to moderate values of Reynolds number. Unfortunately, due to their prohibitive computational cost, such techniques are not feasible for high Reynolds numbers and complex geometries encountered in most industrial aerodynamic flows. In such cases, numerical models based on the solution of the Reynolds-averaged Navier–Stokes (RANS) equations are still needed.

Recently, two new approaches based on RANS equations were proposed: one by Walters and Leylek [28] and the other by Menter et al. [19].

Walters and Leylek [28] developed and implemented a new model for bypass and natural transition prediction based on the RANS equations. It uses an eddy-viscosity RANS framework which is easily implemented into existing in-house or commercial CFD codes. There are two major concepts embodied in Walters and Leylek's approach. The first is the use of a new transport equation to represent the growth of nonturbulent, streamwise fluctuations in the pretransitional boundary layer, an idea that builds upon the work of Mayle and Schulz [29]. The second is the incorporation of fluctuation growth due to a splat mechanism, as proposed by Volino [30]. Walters and Leylek's [28] transition model has been validated by test cases of fully developed channel flow, flat-plate boundary layer with varying levels of freestream turbulence, and a modern, highly loaded turbine airfoil with significant variation of freestream turbulence. It is suggested that this approach has promising potential for transitional flow prediction in engineering application [28].

Menter's $\gamma$-$Re_\theta$ Transition Model [19] has been implemented in the commercial CFD code CFX12, which was used for transition simulation on the natural laminar flow nacelle in this study.

Menter's model, known as the $\gamma$-$Re_\theta$ Transition Model [19], is becoming increasingly accepted for transition prediction in academia and industry. The model involves solving a modified version of the shear stress transport (SST) $k$-$\omega$ turbulence model together with two additional transport equations for turbulence intermittency, $\gamma$, to trigger transition, and for transported transition momentum thickness Reynolds number, $\tilde{Re}_{\theta t}$. The transport transition Reynolds number requires specification of the transition onset momentum Reynolds number in the freestream $Re_{\theta t}$, based on an empirical correlation given by Langtry and Menter [18].

Menter's $\gamma$-$Re_\theta$ Transition Method uses local variables for prediction and therefore is compatible with the modern CFD techniques such as unstructured grids and massively parallel execution. In addition, it does not negatively affect the convergence of the solver [18]. It has been validated over a number of aerodynamic cases, including 2-D airfoils, three-element flaps, a 3-D transonic wing and a full helicopter configuration [18]. The good agreement with the available experimental data indicates that this model is a significant step forward in engineering transition modeling [19], and it is suitable for external aerodynamic applications. Currently, this model accounts for the transition due to freestream turbulence intensity, pressure gradients and separation. The main limitations are lack of consideration of crossflow instabilities, streamwise curvature, freestream turbulent length scale, and high-speed flow correlations (compressibility effect). Further details of the transition model are described in [19]. The development of the code for a range of engineering applications is presented by Malan et al. [31].

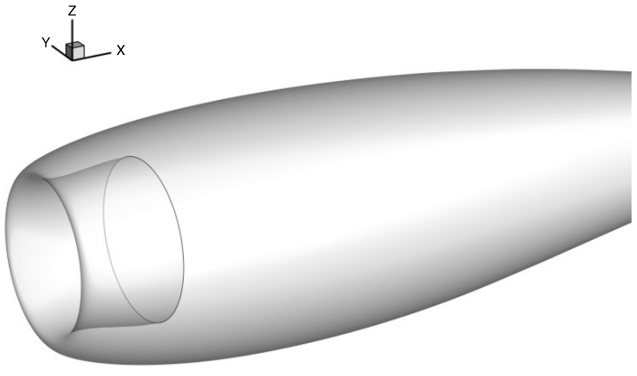


**Fig. 1 Geometry of laminar flow nacelle.**

## II. Methodology

### A. CFD Model

#### 1. Geometry

The geometry of the studied nacelle is shown in Fig. 1. The internal geometry of the nacelle is only represented as far as the fan face. The internal shape of the exit duct is not represented. The external profile of the nacelle between the highlight and the location of the maximum diameter was modified with the aim of extending the region of laminar flow. A scaled nacelle model was employed in wind-tunnel tests and in the CFD simulation.

#### 2. Domain

A three-dimensional rectangular computational domain was created, and the nacelle model was placed inside the domain representing the setup of the wind-tunnel tests. The upstream boundary (domain inlet) was located at 5 chord lengths from the leading edge to avoid excessive decay of the domain inlet turbulence intensity (Tu). The outlet of the domain was located 7 chord lengths away from the nacelle trailing edge.

In any wind-tunnel test program, the interference effects from tunnel walls, model supports, and any other obtrusive hardware could affect the flow. In the work of Lessard [32], the effect of model support and wind-tunnel walls were investigated on a high lift Technology Concept Airplane both computationally and experimentally. The main conclusion from this work is that for predicting overall performance characteristics such as forces and moments, modeling the aircraft in free air was sufficient.

In the wind-tunnel working section, the side walls are perforated to minimize the wall interference effects on the internal flow. In the CFD representation, solid side walls with enlarged domain dimensions (5 chord lengths at each side) were employed to simulate this feature. The rear part of the model supports has been modeled in the CFD model by extending the nacelle trailing edge to the outlet boundary. However, the vertical model postsupport (sting) in the wind-tunnel test section was not included.

#### 3. Mesh and Boundary Conditions

A structured multiblock hexahedral mesh was employed in the domain. An $O$-grid mesh was applied around the nacelle body. The mesh is clustered around the nacelle leading edge, and the wall normal distance to the first data point corresponds to a $y^+$ value less than 1. A wall normal expansion ratio of 1.10–1.12 was employed. The number of nodes in the streamwise direction is chosen to ensure that the aspect ratio of parallel spacing to normal spacing was less than 500. The surface mesh is shown in Fig. 2.

The boundary conditions used were: total pressure and temperature at the domain inlet; freestream static pressure at the outlet; pressure outlet conditions at the fan-plane boundary, to ensure the target mass flow rate is achieved; far-field conditions at the sidewall boundaries; and nonslip condition on the nacelle surface.

A detailed grid-independence study based on transitional flow simulations as a function of both streamwise and normal node number has been performed. This showed that a mesh of 8.6 million hexahedral cells is required to achieve grid-independence and is therefore suitable for transitional flow predictions.

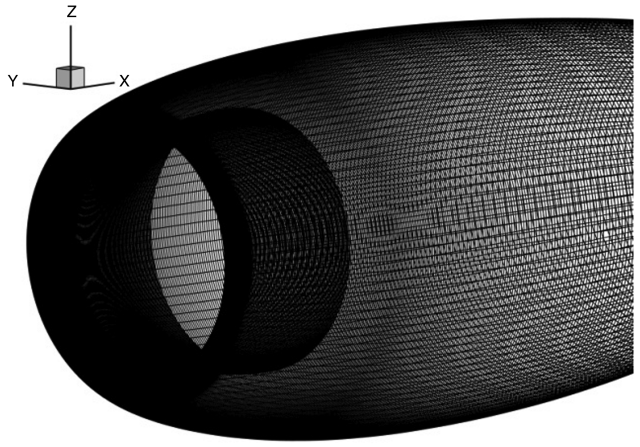


**Fig. 2 Nacelle surface mesh.**

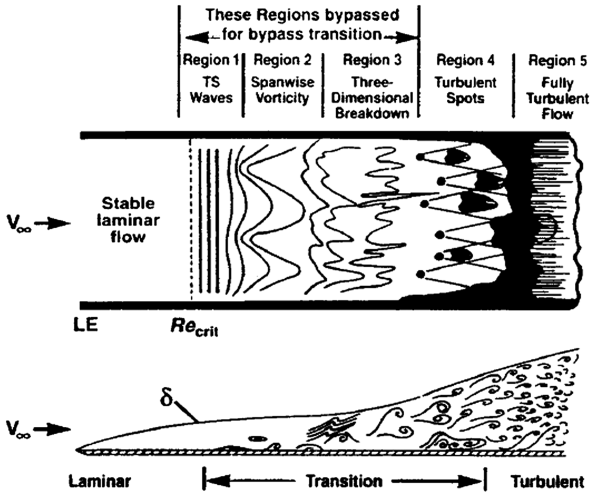


**Fig. 3 Schematic of laminar-turbulent transition in the boundary layer ([39]).**

*4. Solver*

The commercial CFD code CFX12, a parallel, implicitly coupled pressure-based solver that is tuned for industrial CFD applications, was employed in this study in conjunction with Menter's $\gamma$-$Re_\theta$ Transition Model.

The flow is assumed to be compressible and transitional. Total energy is set for heat transfer modeling because the high Mach number ($\sim$0.8) results in significant kinetic energy effects. The high-resolution scheme is used for advection terms and turbulence numerics. This adaptive numerical scheme locally adjusts the discretisation to be as close to second-order as possible to ensure maximum accuracy, while ensuring the physical boundedness of the solution. It is determined that the transition onset location is very sensitive to the advection scheme for the turbulence and transition model equations [19]. Therefore a bounded second-order upwind scheme was chosen for solving the flow equations.

The computational analysis uses the RANS equations with the $k$-$\omega$ SST turbulence model. The SST turbulence model is employed for high-accuracy boundary-layer simulation. It is a hybrid method that couples the standard $k$-$\varepsilon$ and $k$-$\omega$ models in an efficient manner, with the $k$-$\omega$ model used in the near-wall region and the standard $k$-$\varepsilon$ model in the far-field region, blending them together at the interface between the regions. It includes the modeling of transport of shear stress via a modified definition of the turbulent viscosity. Menter's $\gamma$-$Re_\theta$ Transition Model was employed for transitional flow prediction with the constants for the turbulence intermittency equation and the transition momentum thickness Reynolds number equation are set as follows:

$$c_{\gamma 1} = 0.03, \qquad c_{\gamma 2} = 50, \qquad c_{\gamma 3} = 0.5$$
$$\sigma_\gamma = 1.0 \qquad c_{\theta t} = 0.03, \qquad \sigma_{\theta t} = 2.0$$

Steady-state solutions were sought with a maximum residual criterion of $1 \times 10^{-4}$.

### B. Identification of Transition Location in the CFD Simulation

Prediction of transition using CFD simulation produces two values, one for the beginning and the other for the end of the transition process. In contrast, experimental data generally indicate the transition location as being closer to fully turbulent flow. A schematic of the laminar-turbulent transition in the boundary layer on a flat plate at zero-incidence is shown in Fig. 3. The exact beginning and ending transition locations are poorly defined because of the complex mechanism of transition. Nevertheless, the transition location is most often defined as being located in regions 2–4.

In the CFD simulation, there are several output variables that can be used to identify transition: turbulence intermittency $\gamma$, local turbulence intensity (TI), turbulence dissipation rate (TDR), skin friction $C_f$, and changes in the pressure distribution.

In Menter's $\gamma$-$Re_\theta$ Transition Model, turbulence intermittency $\gamma$ is the critical variable used to trigger the switch between laminar and turbulent treatment in the CFX solver [19]. It predicts that the turbulence intermittency will start to increase at a very early stage of the transition region, in regions where the boundary-layer profiles would still be laminar, as shown in region 2 in Fig. 3. TDR and TI start to increase with the onset of turbulence intermittency in the boundary layer and that is controlled by critical value of $Re_\theta$, which is related to the strain rate. Therefore, in the CFD simulation, the initial increase in turbulence intermittency was used to identify the earliest sign of transition within the boundary layer.

The boundary between the final region of transition and fully turbulent flow is not sharply defined by any of the above output variables. It is generally accepted that the end of transition is defined as the location where the maximum value of $C_f$ occurs, which is toward the end of region 4 in Fig. 3.

Therefore, two transition boundary lines around the nacelle circumference, corresponding to the beginning and the end of transition, can be obtained from the CFD solution.

### C. Correction of CFD-Predicted Transition Location

In the CFD simulation, the turbulence intensity specified at the domain inlet can decay quite rapidly with respect to streamwise distance and domain inlet viscosity ratio $R_t$. The decay can be expressed as follows in terms of domain inlet Tu and streamwise distance $x^*$ downstream of the domain inlet [33]:

$$\mathrm{Tu}^* = \mathrm{Tu}\left\{1 + \frac{3\rho V \beta T u^2}{2\mu R_t} \cdot x^*\right\}^{-(0.5\frac{\beta^*}{\beta})} \tag{1}$$

$\beta$ and $\beta^*$ are empirically determined coefficients set as follows: $\beta = 0.09$ and $\beta^* = 0.0828$.

Typically, the larger the viscosity ratio $R_t$ the smaller the turbulent decay rate. However, if $R_t$ specified is too large ($R_t > 100$) the skin friction can deviate significantly from the laminar value. For this reason it is desirable to have a relatively low domain inlet viscosity ratio ($R_t \approx$ 1–10) [33]. In the present study, $R_t = 10$ is used.

The decay is illustrated in Fig. 4 for the datum case with $M = 0.8$, $\alpha = 0°$, mfr $= 0.71$, and $\mathrm{Tu}_{\mathrm{inlet}} = 0.37\%$ showing that the turbulence intensity downstream of the inlet (Tu*) has decreased to 0.114% at the nacelle leading edge (denoted by the black solid line).

Experimental and numerical investigations for a flat plate have verified that freestream turbulence intensity has a significant effect on transitional boundary-layer flow. As Tu increases (but remains under 1%) the transition onset momentum thickness Reynolds number $Re_{\theta t}$ decreases rapidly and consequently the transition location moves upstream. This implies that in the CFD predictions, the decayed freestream turbulence level at the nacelle leading edge results in an overprediction of the laminar flow extension. Therefore, it is

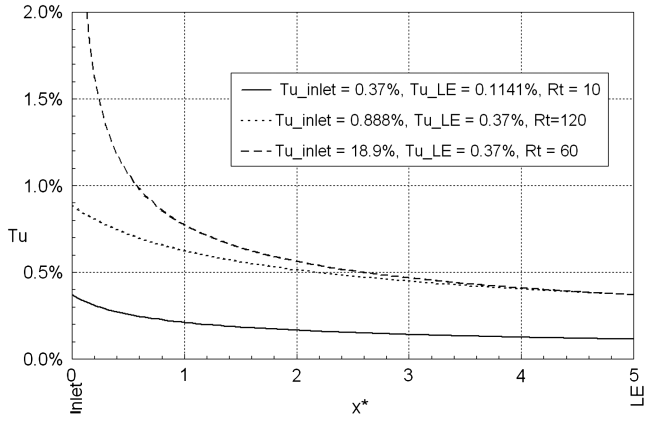


**Fig. 4 Decay of domain inlet Tu as a function of streamwise distance $x^*$ and domain inlet viscosity ratio $R_t$.**

necessary to apply a correction to counteract the decay of turbulence intensity from the domain inlet.

One common technique is to estimate the domain inlet value of turbulence intensity such that at the leading edge of the nacelle the turbulence intensity will decay to the desired value, which, in this case, is 0.37%. However, from Eq. (1), this approach requires either a very large domain inlet viscosity ratio $R_t$ (see the two examples with $R_t = 60$ and 100 in Fig. 4), or the domain inlet boundary to be within one chord length of the nacelle leading edge. The shortcomings of having a large $R_t$ means the skin friction can deviate significantly from the laminar value, as was discussed previously above. When the distance between nacelle leading edge and the domain inlet is short, errors will be introduced into the CFD model, due to pressure wave reflection and interference between the domain inlet boundary and the nacelle body.

Instead, an empirical correction method is adopted here, which can be expressed as follows:

$$\{\text{Transition Location}\}_{\text{after}_{\text{correction}}} = C_{b,e} \cdot \{\text{Transition Location}\}_{\text{CFD}_{\text{Prediction}}} \quad (2)$$

$C_{b,e}$ denotes both $C_b$ and $C_e$ as appropriate empirical correction factors for the beginning and the end of transition, respectively, expressing the effect of Tu on transition onset location $x_t$ i.e., on $Re_t$.

Alternative empirical correlations have been proposed by Abu–Ghannam and Shaw [27], Suzen et al. [34], Mayle and Schulz [29], Menter et al. [19] and Hall and Gibbings [35]. All relate transition onset momentum thickness Reynolds number $Re_{\theta t}$ to freestream Tu. Menter et al.'s correlation for the beginning of transition and Hall and Gibbings' correlation for the end of transition were used, as expressed in Eqs. (3) and (4), respectively

$$Re_{\theta t} = 803.73(Tu + 0.6067)^{-1.027} \quad (3)$$

$$Re_{\theta t} = 320 + \exp(7.7 - 0.4475\text{Tu}) \quad (4)$$

For Tu = 0.37%, and $Tu_{\text{LE}} = 0.114\%$, the correction of $Re_{\theta t}$ for the beginning of transition is 0.732, and for the end of transition is 0.906. The Reynolds number $Re_t$ based on transition onset location $x_t$ is proportional to the square of $Re_{\theta t}$, which gives the corresponding correction factors of $C_b = 0.536$ and $C_e = 0.821$.

It should be emphasized that the correction factors employed here are from the empirical correlations for a flat plate model with zero pressure gradient, and they are not calibrated for nacelle cases. Nevertheless, they still can be used to demonstrate the effect of decay of freestream Tu on the transitional boundary-layer flow on the nacelle surface.

Hereafter, the two transition boundary lines, obtained from the CFD predictions, are corrected using this approach. The experimental data are expected to be located between these two corrected transition boundary lines, lying closer to the end of transition boundary line.

### D. Challenges in CFD Transition Simulations

In the process of conducting transitional flow simulations on the laminar flow nacelle, a number of challenges have been encountered and discussed below.

All the results shown in this section are based on a preliminary study for the case with a Mach number, $M = 0.8$, angle of attack, $\alpha = 0°$ and mass flow ratio, mfr = 0.71. Simulations have been performed for both fully turbulent and transitional flow, and for both steady and transient flow regimes.

#### *1. Body Surface Smoothness*

One requirement for an accurate and successful transition simulation is the smoothness of the model of the surface, which is dependent upon two factors: the CAD model smoothness and the mesh smoothness. A high-quality natural laminar flow nacelle CAD model with more than adequate smoothness for our needs was employed in this study. An appropriate model tolerance in mesh generation is crucial to ensure a smooth surface mesh representing the smooth surface geometry. Preliminary CFD transitional flow simulations were performed with two different meshes, each created in ICEMCFD with model tolerances of $1 \times 10^{-3}$ m and $1 \times 10^{-7}$ m, respectively. Figure 5 shows the CFD-predicted results of surface pressure distribution $C_P$ and skin friction $C_f$ on the nacelle surface. Oscillations can be observed on the $C_P$ and $C_f$ curves with the rougher model with a tolerance of $1 \times 10^{-3}$, as shown in Fig. 5a. These oscillations were eliminated when a smoother model with tolerance of $1 \times 10^{-7}$ was applied, as shown in Fig. 5b.

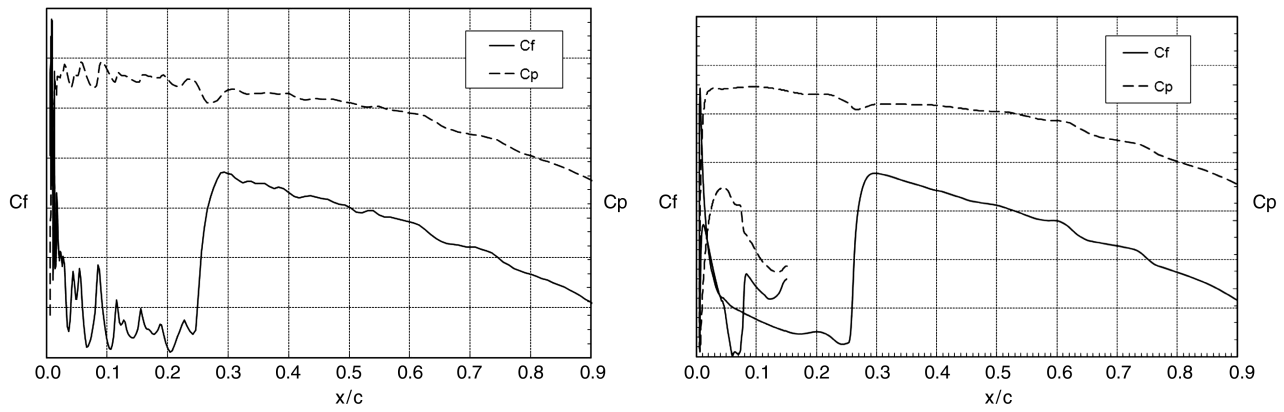


**Fig. 5 Effect of surface mesh smoothness on transition simulation: a) tolerance $1 \times 10^{-3}$ m, and b) tolerance $1 \times 10^{-7}$ m.**

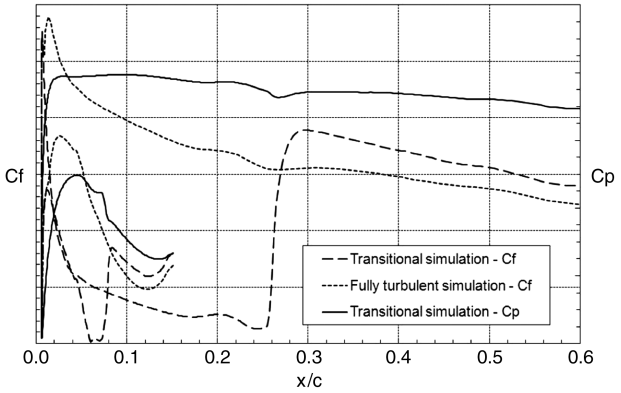


**Fig. 6 Boundary-layer flow separation in nacelle intake flow.**

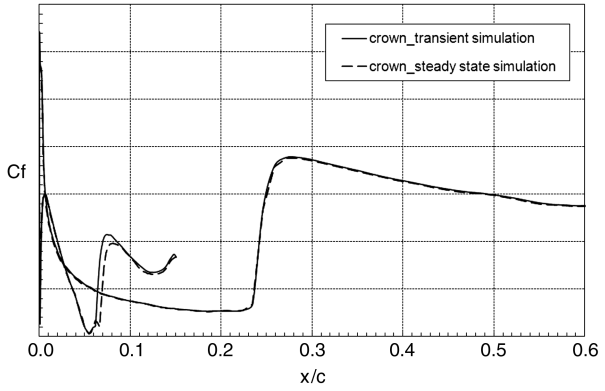


**Fig. 7 Comparison of skin friction $C_f$ between steady-state and transient simulation.**

*2. Intake Flow Separation*

The transitional flow simulation on the laminar flow nacelle exhibited boundary-layer flow separation in the nacelle intake, which can be inferred from both the skin friction and the plateau in surface pressure distribution. This is shown in Fig. 6, in which the $C_P$ and $C_f$ at the nacelle crown section for both the transition and fully turbulent simulations are presented. In the transitional flow simulation separation of the flow was also observed in velocity streamlines in the nacelle intake flow.

An additional issue encountered within the transitional flow simulation is that the targeted maximum residual criterion cannot be met. The moving separation bubble in the nacelle intake flow causes a local lack of maximum residual convergence.

A transient simulation was performed to address this issue, and the results at different time steps were compared with the steady-state simulation at the crown, keel, inboard, and outboard sections of the nacelle surface. A comparison of the stagnation points coordinates on the four specific sections on the nacelle between the steady-state simulation and transient simulation at one time step, as shown in Table 1, indicated that the difference is within one cell scale. Similar results were obtained at other time steps. The comparison of skin friction is shown in Fig. 7. For brevity, only the skin friction at the crown section is presented here. The difference between the results of the steady-state simulation and the transient simulation at one time step is very small, with only a minor difference in the intake flow. Similar results were obtained at the other three sections and also at all other time steps.

The results demonstrate that the small area of unstable flow and resulting lack of tight convergence of the maximum residuals do not significantly change the overall transition behavior on the nacelle outer surface. Therefore, the steady-state simulation with local lack of maximum residual convergence was considered acceptable to be used in the remaining work.

## III. Validation and Discussion

A key parameter in the validation of transitional boundary-layer flow is the domain inlet Tu. The approximate relationship between turbulence Tu and $N$ factor can be expressed as [36]:

$$N = -8.43 - 2.4\,\ell_n(\mathrm{Tu}), \quad \text{for } 0.1\% < \mathrm{Tu} < 1\% \tag{5}$$

This correlation overpredicts laminar flow extent for Tu levels of less than 0.1%.

An $N$ factor of 5 has been assumed for the calculation. The corresponding turbulence intensity Tu = 0.37% was used in all CFD simulation cases.

### A. CFD Validation Cases

The CFD simulation cases chosen for consideration, as shown in Table 2, are based on the availability of experimental data for validation. Case 1 is referred to as the datum case and case 2 as the transonic case.

### B. Validation Results

In the wind-tunnel experiments, static pressure measurements were taken at three nacelle radial planes: 23, 90, and 157°, where the radial planes are measured positively from the crown section (0°) to the inboard section (90°). Comparisons of these with the CFD predictions are presented in this paper. In addition, the corrected transition boundary lines from CFD prediction are also compared with experimental data.

The CFD-predicted surface pressure distribution $C_p$, and the corresponding experimental data for the datum case relative to the fractional nacelle chord length are shown in Fig. 8. The CFD-predicted skin friction coefficient $Cf$ is also presented.

For the external flow, from the leading edge to about 45% of the nacelle chord, the CFD prediction is in close agreement with the experimental data at all three radial planes. It is known that the growth of unstable T-S waves is sensitive to the boundary-layer profile. In a favorable pressure gradient the velocity profile gets fuller and the amplification of T-S waves in the streamwise direction is reduced. With adverse pressure gradients the T-S waves amplify more rapidly leading to earlier transition [37,38]. In the datum case, the sharp change in pressure coefficient $C_p$ on the external surface predicted by CFD corresponds to the transition location indicated by the sudden increase in skin friction coefficient $C_f$. This implies that the adverse pressure gradients lead to onset of transition. However, this localized change in $C_p$ gradient is not noticeable in the experimental data as the pressure tapping pitch is not adequate to capture this detail. Figure 8 also shows differences in the aft part of the external flow. This is possibly due to the model postsupport (sting) not being present in the CFD model. The sting has some effect on the local pressure on the nacelle surface [32]. However, the pressure differences in the downstream flow is away from the transition onset location, which means it will only affect the turbulent

**Table 1 Comparisons of stagnation points between steady-state and transient simulation**

| | Transient simulation | Steady-State simulation | Difference |
|---|---|---|---|
| Crown | (0.005944, 0.120322, 0) | (0.005946, 0.120317, 0) | (2e − 6, 5e − 6, 0) |
| Keel | (−0.004871, −0.11414, 0) | (−0.005006, −0.114920, 0) | (1.35e − 4, 7.8e − 4, 0) |
| Inboard | (0.000593, 0, 0.116623) | (0.0006, 0, 0.116609) | (7e − 6, 0, 1.4e − 5) |
| Outboard | (0.00015, 0, −0.11794) | (0.00015, 0, −0.11794) | (0, 0, 0) |

**Table 2 CFD validation program for cruise cases**

| Case number | Mach number | $\alpha$, ° | mfr |
|---|---|---|---|
| Case 1 | 0.8 | 0 | 0.71 |
| Case 2 | 0.88 | 0 | 0.71 |
| Case 3 | 0.8 | −2 | 0.71 |
| Case 4 | 0.8 | 0 | 0.75 |
| Case 5 | 0.8 | 0 | 0.65 |
| Case 6 | 0.8 | 0 | 0.60 |

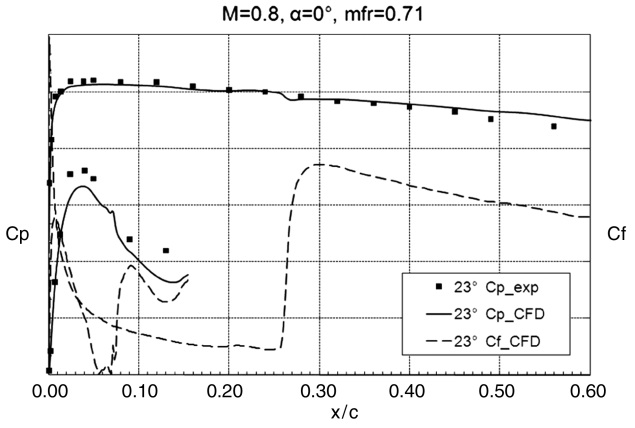


a)

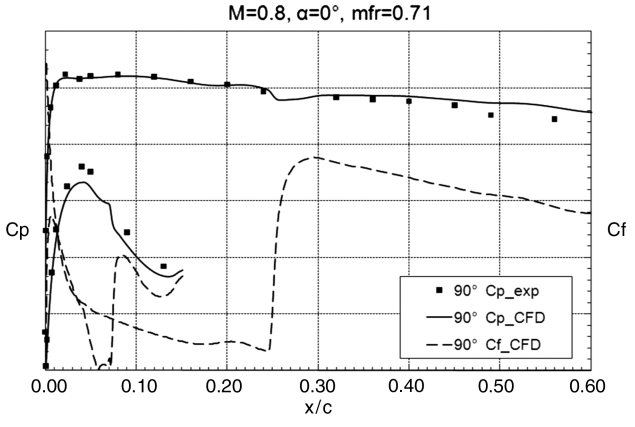


b)

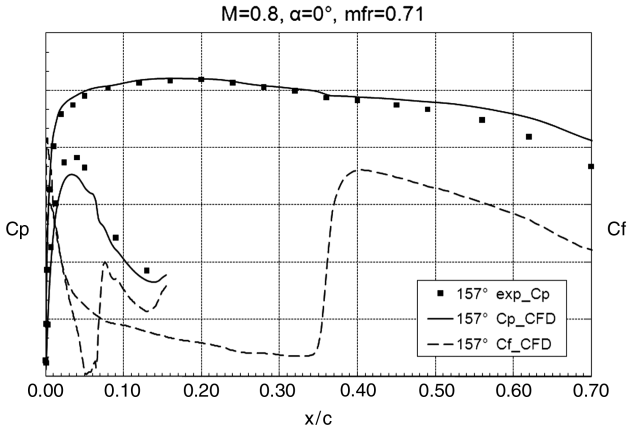


c)

**Fig. 8 Comparison of CFD-predicted $C_p$ and $C_f$ with the experimental $C_p$ data for the datum case ($M = 0.8$, $\alpha = 0°$, $\mathrm{mfr} = 0.71$).**

boundary-layer flow, not the laminar and transitional boundary-layer flow, and hence the transition location.

For the nacelle intake, Fig. 8 shows significant difference between the predicted and experimental results. This is due to the spinner being present in the experimental setup but omitted in the CFD model. The spinner reduces the cross-sectional area of the intake and consequently reduces the local pressure.

A comparison between the CFD-predicted and the experimental pressure distributions are shown in Fig. 9 for mass flow ratios of 0.65 and 0.75 and in Fig. 8 for a mass flow ratio of 0.71. For brevity, only the data at the 23° radial planes are presented in Fig. 9. Similar results are seen at the other two locations tested. The CFD predictions agree with wind-tunnel test data, and the predicted transition locations coincide with the steep gradients in the pressure, for a range of mass flow ratios.

Figure 10 shows that the major effect of varying mass flow ratio is on the surface pressure coefficient, $C_p$, close to the nacelle leading edge. As the mass flow ratios are reduced the pressure becomes more negative in the external flow regions close to the nacelle leading edge. This gives a stronger adverse pressure gradient and consequently an earlier transition to turbulence, as shown in their transition location $C_f$ curves.

Comparisons of experimental and predicted transition locations for cases with mass flow ratios of 0.75, 0.65, and 0.60 are presented in Figs. 11–13, respectively. The CFD-predicted boundary lines for both the beginning and the end of transition are illustrated along with the transition boundary lines defined during the chemical sublimation tests performed in the natural laminar flow nacelle wind-tunnel program.

Figures 11–13 show that, in general, the CFD prediction trends agree with the experiments. The laminar flow extent is less over that

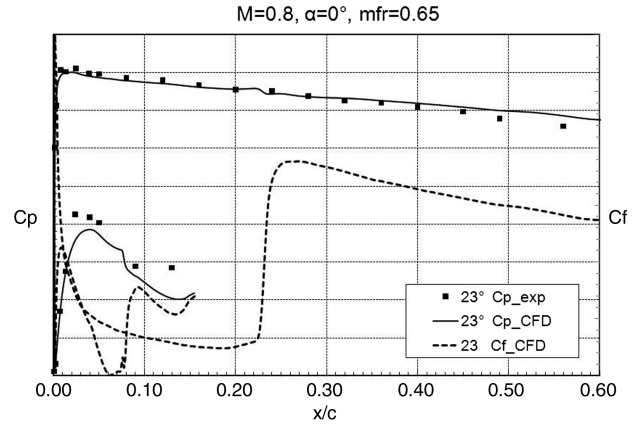


a)

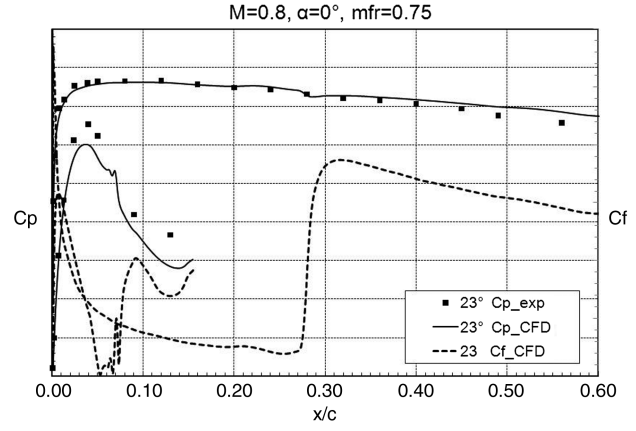


b)

**Fig. 9 Comparison of CFD-predicted $C_p$ and $C_f$ with the experimental $C_p$ data for two mfr cases: a) $M = 0.8$, $\alpha = 0°$, $\mathrm{mfr} = 0.65$, and b) $M = 0.8$, $\alpha = 0°$, $\mathrm{mfr} = 0.75$.**

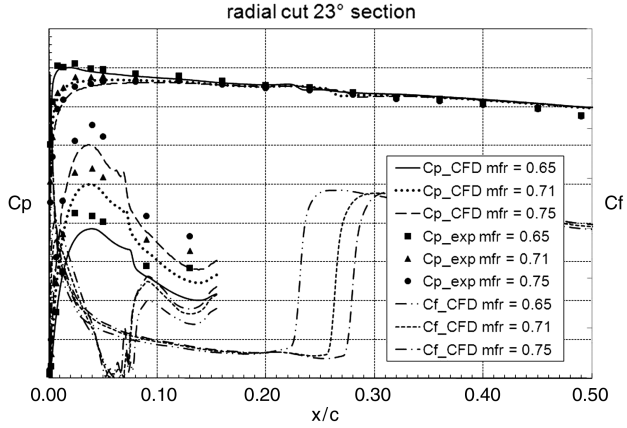


**Fig. 10 Comparison of CFD-predicted $C_p$ and $C_f$ with the experimental $C_p$ data for a series of mfr cases.**

part of the nacelle where the maximum profile depth is the thinnest (0–90°) compared with where the maximum profile depth is the thickest (180–270°). The maximum nacelle profile depth is thinnest at the plane of the pylon, which coincides with the inboard section. The maximum nacelle profile depth is thickest between the keel and outboard sections. It is also noted that at the thinnest part of the nacelle the transition boundary from the wind-tunnel tests either maintains a mean position between the two CFD prediction boundaries (Fig. 13) or is located near the nacelle leading edge (Figs. 11 and 12). This shows the sensitivity of transition to the cross-sectional profile at the thinnest nacelle sections.

These results show that, in general, Menter's $\gamma$-$Re_\theta$ Transition Model is capable of capturing the effect of mass flow ratio on transition in the presence of transonic flow.

Contours of isentropic Mach number on the nacelle surface for the transonic case with $M = 0.88$, $\alpha = 0°$, and mfr $= 0.71$ is shown in Fig. 14. Strong shockwaves and laminar boundary-layer separation occurred at 10–20% chord around the whole nacelle. The strongest

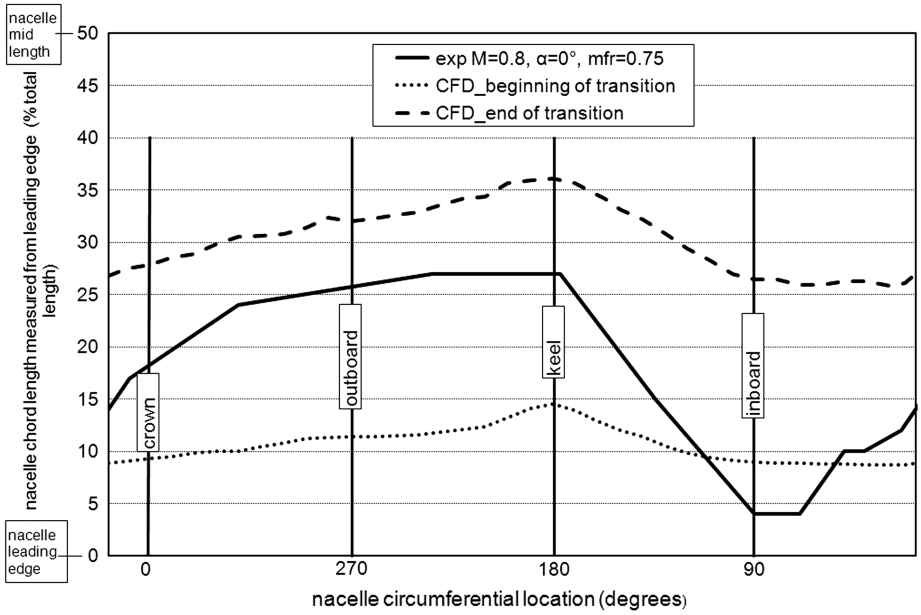


**Fig. 11 Transition location validation for cruise case $M = 0.8$, $\alpha = 0°$, mfr $= 0.75$.**

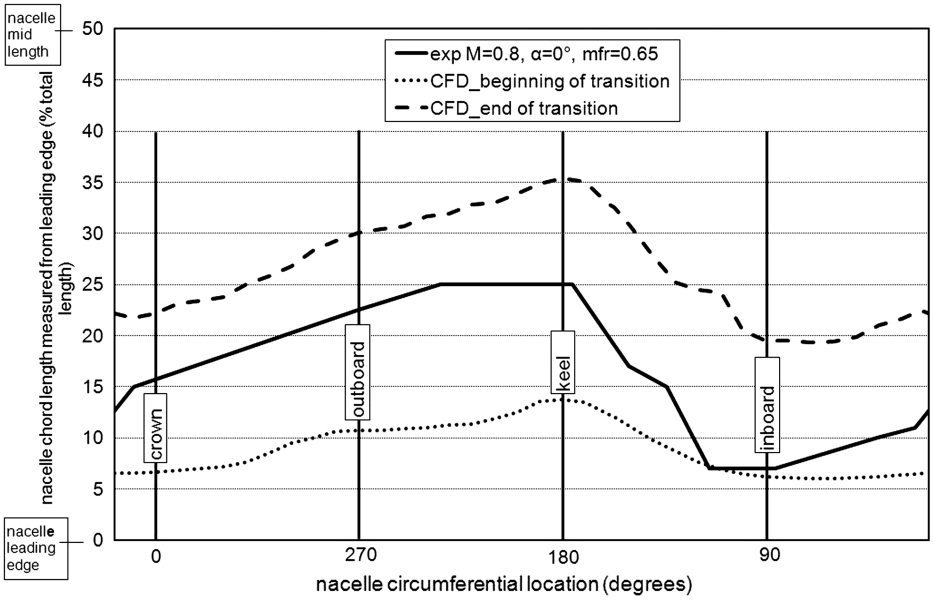


**Fig. 12 Transition location validation for cruise case $M = 0.8$, $\alpha = 0°$, mfr $= 0.65$.**

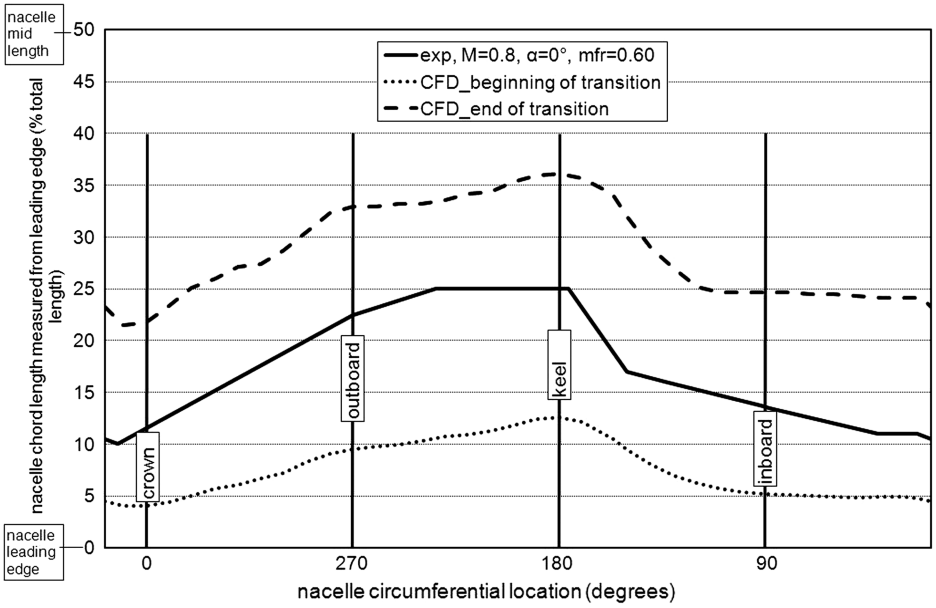


**Fig. 13 Transition location validation for cruise case $M = 0.8$, $\alpha = 0°$, mfr $= 0.60$.**

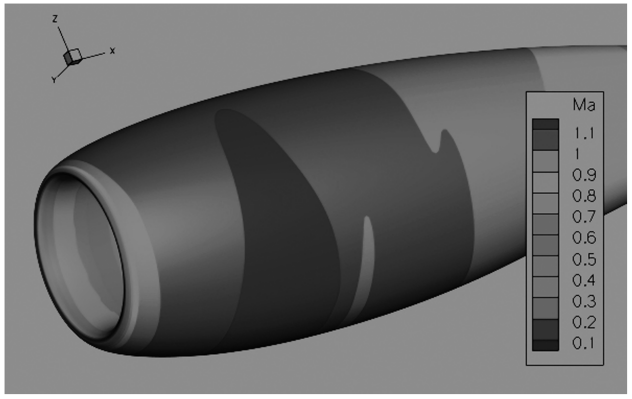


**Fig. 14 Contour of isentropic Ma on nacelle surface for Mach number case $M = 0.88$, $\alpha = 0°$, mfr $= 0.71$.**

shockwaves appear around the keel section with a maximum surface isentropic Mach number of 1.13, which results in earlier transition.

The corresponding transition boundary lines and the comparison of the CFD-predicted pressure distributions with the experimental data for the same transonic case are shown in Figs. 15 and 16 respectively. The comparison shown in Fig. 16 of the CFD-predicted pressure distributions with the experimental data at three radial planes shows good agreement. However, as discussed above, the transition location from the test data on the thinnest part of the nacelle is more sensitive to the upstream flow parameters, with an abrupt reduction of the laminar flow extent. The large discrepancy between the CFD prediction and experimental results, as shown in Fig. 15, may imply that the grid around the nacelle leading edge is not fine enough to capture any small shock in that region: no shocks are evident in the $C_p$ distribution of the CFD solution (see Fig. 16b). Above a Mach number of 0.8, the unstable flow, shock waves and separation intensify the sensitivity of the boundary-layer transition to the local flow instability where the maximum profile depth is thinnest. Therefore, a refined mesh around the nacelle leading edge is required for correct transition prediction using Menter's method.

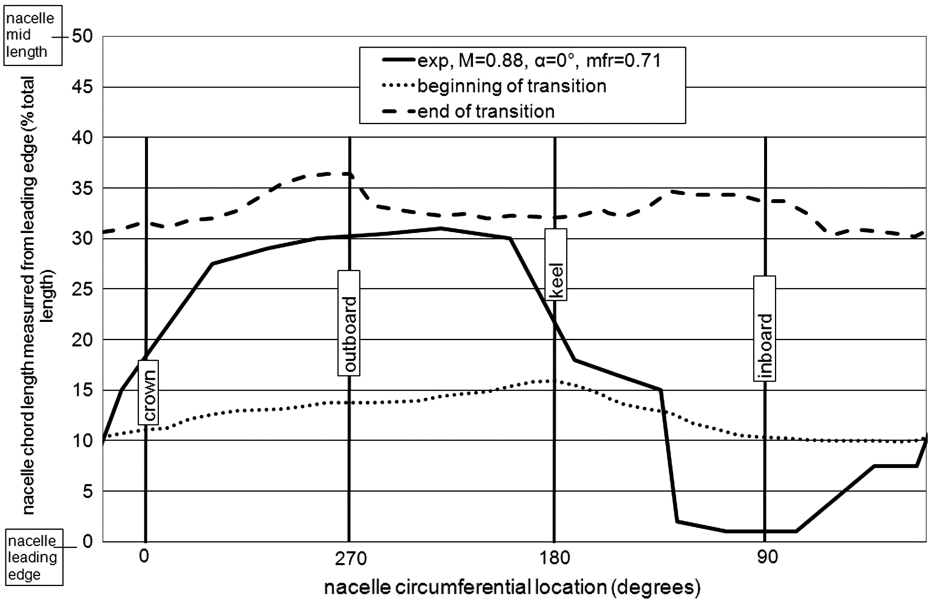


**Fig. 15 Transition location validation for cruise case $M = 0.88$, $\alpha = 0°$, mfr $= 0.71$.**

However, where the maximum profile depth is thickest, with more favorable conditions for laminar flow, the experimental data show that there is no laminar flow break down at the nacelle leading edge.

Both the CFD prediction and experimental results show an improvement in laminar flow extent at this higher Mach number. High subsonic Mach numbers have a complex effect on the transition location. In the absence of shockwaves and laminar flow separation, the higher Mach numbers cause downstream movement of the transition location. However, in the presence of shockwaves or laminar flow separation, or both, the T-S waves are significantly amplified, which hastens transition. The final results, therefore, are the combination of these two contrary effects.

A comparison between the CFD-predicted and the experimental pressure distributions are shown in Fig. 17 for an angle of attack of $-2°$ and in Fig. 8 for an angle of attack of 0°. For clarity, the $C_f$ data for $\alpha = 0°$ have been included in Fig. 17.

At both sections presented, the CFD predictions for $C_p$ agree with the experimental data. At radial plane 23° a negative incidence angle moves the stagnation point outwards toward the external surface, resulting in extended laminar flow, as shown in Fig. 17a. Conversely, there is reduced laminar flow at radial plane 157°, as shown in Fig. 17b.

The results of this study indicate that Menter's $\gamma$-$Re_\theta$ Transition Model, as implemented in CFX12, is capable of predicting the transitional flow behavior of nacelle cases with a small angle of attack, in which the crossflow velocity is much lower compared with the streamwise flow velocity, and the T-S disturbance still dominates the transition in the boundary layer.

### C. Assessment of Prediction Capability of the Menter's $\gamma$-$Re_\theta$ Transition Model

In general, the CFD simulations agreed with the experiments in all cases for Mach numbers ranging from 0.8 to 0.88, mass flow ratios ranging from 0.60 to 0.75, and angles of attack ranging from $-2$ to 0°. The validation results indicate that Menter's $\gamma$-$Re_\theta$ Transition Model, as implemented in CFX12, is appropriate to consider for transition predictions on nacelle surfaces and when the turbulence levels are low (Tu $< 1\%$). Nevertheless, there are still some limitations in both the CFD model and the implementation of Menter's $\gamma$-$Re_\theta$ Transition Model in the nacelle cases, which, to some extent, cause the discrepancy between CFD results and experimental data on natural laminar boundary-layer transition.

#### 1. *Limitations in Menter's $\gamma$-$Re_\theta$ Transition Model*

Menter's $\gamma$-$Re_\theta$ Transition Model is a correlation-based model, and the flow physics of the transition process are expressed within the

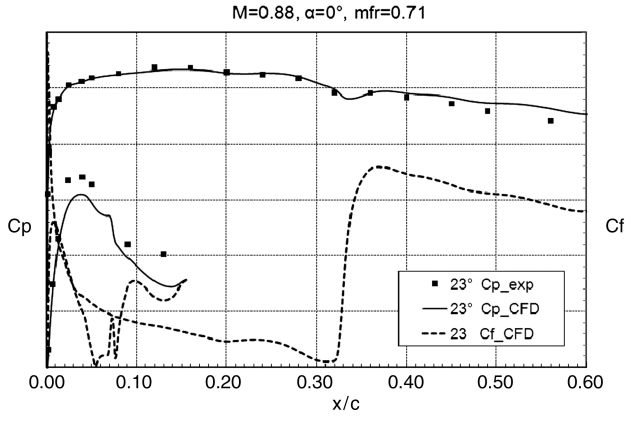


a)

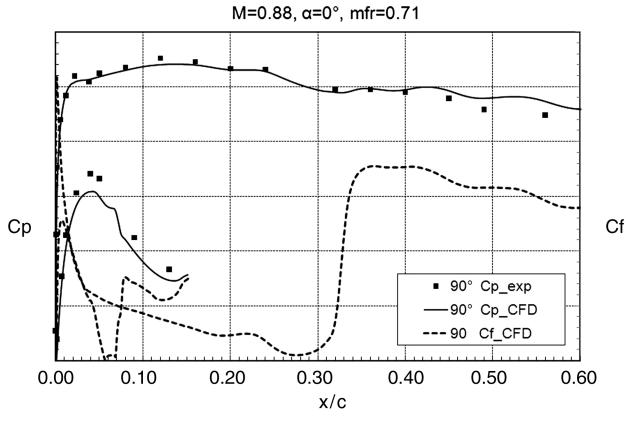


b)

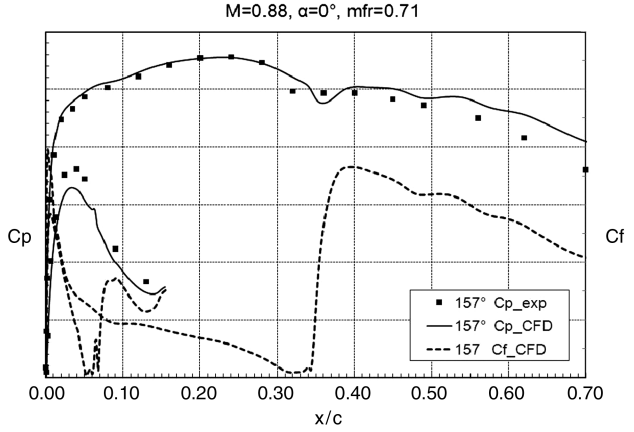


c)

**Fig. 16 Comparison of CFD-predicted $C_p$ and $C_f$ with the experimental $C_p$ data for the transonic case ($M = 0.88$, $\alpha = 0°$, $\mathrm{mfr} = 0.71$).**

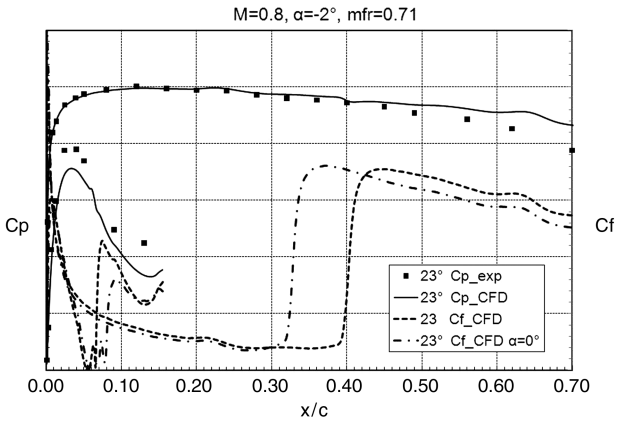


a)

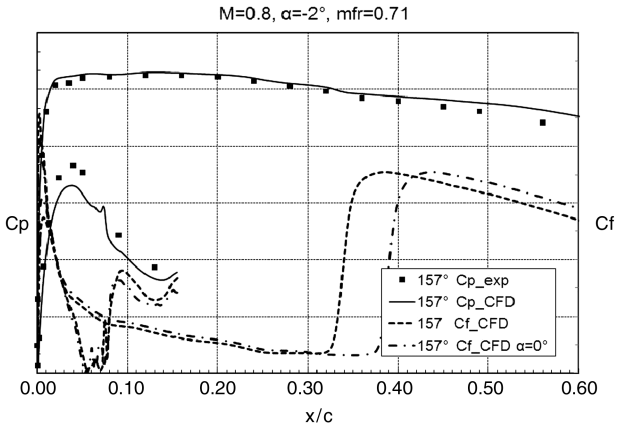


b)

**Fig. 17 Comparison of CFD-predicted $C_p$ and $C_f$ with the experimental $C_p$ data for an incidence case ($M = 0.8$, $\alpha = -2°$, $\mathrm{mfr} = 0.71$).**

experimental correlations provided to the model [19]. The present model formulation is a starting point for the inclusion of additional effects and flow regimes [19], such as roughness, freestream turbulent length scale, streamline curvature, crossflow transition, and compressibility. Many of these additional parameters are particularly applicable to nacelles, for example, compressibility effects, surface roughness, and streamline curvature, which are not included in the current formulation of Menter's $\gamma$-$Re_\theta$ Transition Model.

From the validation cases discussed in this study, it can be seen that above Mach 0.8, Menter's $\gamma$-$Re_\theta$ Transition Model works well where the nacelle maximum profile depth is thickest. However, where the nacelle maximum profile depth is thinnest, where the boundary-layer transition is more sensitive to the local unstable flow, a refined mesh is required to capture any small shock waves which might influence the transition.

For the incidence angle cases with velocity in all three coordinate directions, Menter's $\gamma$-$Re_\theta$ Transition Model is only capable of predicting transition behavior provided the crossflow velocity is much lower compared with the streamwise flow velocity, which means that the T-S wave instability is still the dominant transition mechanism.

Menter's $\gamma$-$Re_\theta$ Transition Model behaves equally well for all the mass flow ratios tested in this study. However, the method shows sensitivity to the cross-sectional profile, in particular where the nacelle is thinnest and transition can "jump" to the leading edge.

#### 2. *Other Limitations of the CFD Model*

The wind-tunnel model intentionally included some minor surface roughness over some portions of the nacelle. This roughness was not included in the CFD model. The CFX12 solver has updated its rough wall treatment with correlations for the effect of roughness on transition onset based on a fixed geometric roughness height [33]. Current work is extending the modeling to include surface roughness.

A second influential factor is the decay of domain inlet turbulence intensity, which also has significant effect on transition boundaries. A more accurate empirical correlation relating turbulence intensity and transition Reynolds number for nacelle application is required.

A third factor is the configuration of the experiments in the wind tunnel, especially the model postsupport (sting), which is not included in the CFD model. Investigation of the interference effect of the model postsupport (sting) on the flowfield by Lessard [32] showed that it has an influence on the local flow physics. The discussion in the validation of datum case shows that the model postsupport (sting) does have an effect on the nacelle surface pressure distribution further downstream in the turbulent boundary layer. A spinner was also present in the wind-tunnel tests and only included in some of the off-design CFD modeling. However, the spinner only influences the flow in the intake and has negligible effect on the external flow.

In addition, wind-tunnel noise and vibration, which may have influenced the experimental test results, are not taken into account in this study.

## IV. Conclusions

In this study, Menter's $\gamma$-$Re_\theta$ Transition Model, as implemented in CFX12 solver, was used for transition prediction on a natural laminar flow nacelle. The implementation of the model was discussed in detail, including the mesh generation and application of the boundary conditions, CFD model creation, and the numerical solver.

Some challenges associated with this type of transitional flow simulation have been identified and discussed. The CFD model surface smoothness is a crucial influential factor for an accurate and successful transition simulation. The small area of laminar boundary-layer separation in the nacelle intake and resulting lack of tight convergence of the maximum residuals does not change the overall transition behavior on the nacelle external surface. This means the steady-state simulation is suitable for transition prediction on the nacelle.

The identification and correction of transition location in the CFD simulation was also discussed in this study. Turbulence intermittency and skin friction have been identified to be the critical indicators for the beginning and the end of transition, respectively. The CFD-predicted transition locations were corrected to counteract the effects caused by the decay of domain inlet turbulence intensity.

CFD simulations were performed for a series of cruise cases with Mach numbers ranging from 0.8 to 0.88, angles of attack from $-2$ to $0°$, and mass flow ratios from 0.60 to 0.75. The CFD results were then compared with the surface pressure distributions and the chemical sublimation defined transition boundaries obtained in the wind-tunnel tests. In general, the CFD simulations agreed with the experiments. This indicates that, under most flow conditions considered in this study, Menter's $\gamma$-$Re_\theta$ Transition Model as implemented in CFX12 is appropriate in predicting boundary-layer transition on nacelle surfaces at typical cruise conditions.

However, the deviation of the CFD predictions from the experimental data in some cases indicates that Menter's $\gamma$-$Re_\theta$ Transition Model formulation as implemented in CFX12 is still limited for its application in nacelle cases. Above a Mach number of 0.8, the sensitivity of transition to the cross-sectional profile observed in experimental results indicated a need for a highly refined mesh. Also, Menter's $\gamma$-$Re_\theta$ Transition Model formulation is only capable of the prediction of transition in three-dimensional boundary-layer flow as long as the crossflow velocity is much lower than the streamwise flow velocity, and the T-S disturbance transition still dominates. This is shown by the incidence case ($\alpha = -2°$) considered in this study, which gives good comparison with the experimental results.

Suggestions for further improvement in Menter's $\gamma$-$Re_\theta$ Transition Model are consideration of the effects of crossflow transition and compressibility. Some of the discrepancies are also related to the modeling approximations in the current study, such as neglecting surface roughness, the spinner, and the model postsupport (sting).

## Acknowledgments

This project was cofunded by the Technology Strategy Board's Collaborative Research and Development program, following an open competition. The Technology Strategy Board is an executive body established by the government of the United Kingdom to drive innovation. It promotes and invests in research, development, and the exploitation of science, technology, and new ideas for the benefit of business, increasing sustainable economic growth in the United Kingdom and improving quality of life.

The authors would like to acknowledge the support and technical contributions from Srinivasan Raghunathan and John Watterson at Queen's University Belfast, and Hui Yao at Bombardier Belfast.

## References

[1] "2008 Addendum to the Strategic Research Agenda," Advisory Council for Aeronautics Research in Europe (ACARE), 2008.

[2] Joslin, R. D., "Aircraft Laminar Flow Control," *Annual Review of Fluid Mechanics*, Vol. 30, 1998, pp. 1–29. doi:10.1146/annurev.fluid.30.1.1

[3] Brooks, C. W. Jr., and Harris, C. D., "Result of LFC Experiment on Slotted Swept Supercritical Airfoil in Langley's 8-Foot Transonic Pressure Tunnel," NASA CP 2487, 1987, pp. 453–459.

[4] Joslin, R. D., "Evolution of Stationary Crossflow Vortices in Boundary Layers on Swept Wings," *AIAA Journal*, Vol. 33, No. 7, 1995, pp. 1279–1285. doi:10.2514/3.12551

[5] Bobbitt, P. J., Harvey, W. D., Harris, C. D., and Brooks, C. W. Jr., *The Langley 8-foot Transonic Pressure Tunnel Laminar-Flow Control Experiment. In NLF and LFC*, Springer–Verlag, New York, 1992, pp. 247–411.

[6] Redeker, G., Horstmann, K. H., Koester, H., and Quast, A., "Investigations on High Reynolds Number Laminar Flow Airfoils," *Journal of Aircraft*, Vol. 25, No. 7, 1988, pp. 583–590. doi:10.2514/3.45627

[7] Haynes, T. S., and Reed, H. L., "Computations in Nonlinear Saturation of Stationary Crossflow Vortices in a Swept-Wing Boundary Layer," AIAA Paper 96-0182, 1996.

[8] Reneaux, J., and Blanchard, A., "The Design and Testing of an Airfoil with Hybrid Laminar Flow Control," *1st Proceeding of the European Forum on Laminar Flow Technology*, DGLR, Hamburg, Germany, 1992, pp. 164–174.
[9] Schmitt, V., Reneaux, J., and Priest, J., "Maintaining Laminarity by Boundary Layer Control," *Sci. Tech. Act.*, ONERA, Toulouse, France, March 1993, pp. 13–14.
[10] Bobbitt, P. J., Ferris, J. C., Harvey, W. D., and Goradia, S. H., "Hybrid Laminar Flow Control Experiment Conducted in NASA Langley 8-foot Transonic Pressure Tunnel," NASA TP 3549, 1996.
[11] Lamb, M., Abeyounis, W. K., and Atterson, J. C. Jr., "Nacelle/Pylon/Wing Integration on a Transport Model with a Natural Laminar Flow Nacelle," NASA Technical Paper 2439, 1985.
[12] Mullender A. J., and Poll, I. A., "Natural and Hybrid Laminar Flow Control for Aero-Engine Nacelles," SAE 952016, 1995.
[13] Barry, B., Parke S. J., Bown, N. W.., Riedel, H., and Sitzmann, M., "The Flight Testing of Natural and Hybrid Laminar Flow Nacelles," ASME Paper No. 94-GT-408, 1994, pp. 1–14.
[14] Riedel, H., Horstmann, K. -H., Ronzheimer, A., and Sitzmann, M., "Aerodynamic Design of a Natural Laminar Flow Nacelle and the Design Validation by Flight Testing," *Aerospace Science and Technology*, Vol. 2, No. 1, 1998, pp. 1–12. doi:10.1016/S0034-1223(98)80001-8
[15] Lamb, M., Abeyounis, W. K., Patterson, J. C, Jr., and Re, R. J., "Natural Laminar Flow Nacelle for Transport Aircraft," NASA Technical Paper 14949, 1988.
[16] Younghans, J. L., and Lahti, D. J., "Analytical and Experimental Studies on Natural Laminar Flow Nacelles," AIAA Paper 84-0034, Jan. 1984.
[17] Radespiel, R., Horstmann, K., and Redeker, G., "Feasibility Study on the Design of a Laminar Flow Nacelle," *27th Aerospace Sciences Meeting*, AIAA Paper 89-0640, 1989.
[18] Langtry, R. B., and Menter, F. R., "Transition Modelling for General CFD Applications in Aerodynamics," *43rd AIAA Aerospace Science Meeting and Exhibit*, AIAA Paper 2005-522, 2005.
[19] Menter, F. R., Langtry, R. B., Likki, S. R., Suzen, Y. B., Huang, P. G., and Volker, S., "A Correlation-based Transition Model Using Local Variables—Part 1: Model Formulation," *Journal of Turbomachinery*, Vol. 128, July 2006, pp. 413–422. doi:10.1115/1.2184352
[20] Menter, F. R., Langtry, R. B., Likki, S. R., Suzen, Y. B., Huang, P. G., and Volker, S., "A Correlation-Based Transition Model Using Local Variables, Part 2: Test Cases and Industrial Applications," *Journal of Turbomachinery*, Vol. 128, No. 3, July 2006, pp. 423–434. doi:10.1115/1.2184353
[21] Savill, A. M., "By-Pass Transition Using Conventional Closures," *Closure Strategies for Turbulent and Transitional Flows*, edited by B. Launder, and N. Sandham, Cambridge Univ. Press, Oxford, England, UK, 2002, pp. 464–492.
[22] Westin, K. J. A., and Henkes, R. A. W. M., "Application of Turbulence Models to Bypass Transition," *Journal of Fluids Engineering*, Vol. 119, No. 4, 1997, pp. 859–866. doi:10.1115/1.2819509
[23] De Palma, P., "Accurate Numerical Simulation of Compressible Turbulent Flows in Turbo-Machinery," *AIAA Journal*, Vol. 40, No. 4, 2002, pp. 702–708. doi:10.2514/2.1702
[24] Wilcox, D. C., *Turbulence Models for CFD*, DCW Industries Inc., La Cañada, CA, 1998, pp. 192–218.
[25] Cutrone, L., De Palma, P., Pascazio, G., and Napolitano, M., "An Evaluation of Bypass Transition Models for Turbo-Machinery Flows," *International Journal of Heat and Fluid Flow*, Vol. 28, No. 1, 2007, pp. 161–177. doi:10.1016/j.ijheatfluidflow.2006.02.031
[26] Stock, H. W., and Haase, W., "Navier–Stokes Airfoil Computations with $e^N$ Transition Prediction Including Transitional Flow Regions," *AIAA Journal*, Vol. 38, No. 11, 2000, pp. 2059–2066. doi:10.2514/2.893
[27] Abu–Ghannam, B. J., and Shaw, R., "Natural Transition of Boundary Layers—The Effects of Turbulence, Pressure Gradient, and Flow History," *Journal of Mechanical Engineering Science*, Vol. 22, No. 5, 1980, pp. 213–228. doi:10.1243/JMES_JOUR_1980_022_043_02
[28] Walters, D. K., and Leylek, J. H., "A New Model for Boundary Layer Transition Using a Single-Point RANS Approach," *Journal of Turbomachinery*, Vol. 126, No. 1, Jan. 2004, pp. 193–202. doi:10.1115/1.1622709
[29] Mayle, R. E., and Schulz, A., "The Path to Predicting Bypass Transition," *Journal of Turbomachinery*, Vol. 119, No. 3, 1997, pp. 405–411.
[30] Volino, R. J., "A New Model for Free-Stream Turbulence Effects on Boundary Layers," *Journal of Turbomachinery*, Vol. 120, No. 1, 1998, pp. 613–620.
[31] Malan, P., Suluksna, K., and Juntasaro, E., "Calibrating the $\gamma$-$Re_\theta$ Transition Model for Commercial CFD," AIAA Paper 2009-1142, Jan. 2009.
[32] Lessard, W. B., "Analysis of Post-Support and Wind-Tunnel Wall Interference on Flow Field about Subsonic High-Lift High-Speed Research Configuration," NASA TP-2000-210555, 2000.
[33] "CFX Transition Model," CFX Manual, 2010.
[34] Suzen, Y. B., Xiong, G., and Huang, P. G., "Predictions of Transitional Flows in Low-Pressure Turbines Using an Intermittency Transport Equation," AIAA Paper No. 2000-2654, 2000.
[35] Hall, D. J., and Gibbings, J. C., "Influence of Stream Turbulence and Pressure Gradient on Boundary-Layer Transition," *Journal of Mechanical Engineering Science*, Vol. 14, 1972, pp. 134–146. doi:10.1243/JMES_JOUR_1972_014_019_02
[36] Mack, L. M., "Transition Prediction and Linear Stability Theory," *Laminar-Turbulent Transition*, AGARD CP-224, 1977, pp. 1–22.
[37] Hefner, J. N., and Bushnell, D. M., "Application of Stability Theory to Laminar Flow Control," *AlAA 12th Fluid and plasma Dynamics Conference*, AIAA Paper 79-1493, 1979.
[38] Fashifar, A., and Johnson, M. W., "An Improved Boundary Layer Transition Correlation," ASME Paper No. ASME-92-GT-245, 1992.
[39] White, F. M., *Viscous Fluid Flow*, McGraw–Hill, New York, 1974, p. 376.

P. Tucker
*Associate Editor*